How to Cite: Baimuratova, R.K., Bazargulov, R.N., Kleinikova, S.A., Zolotukhina, E.V., Gor'kov, K.V., Zhidkov, M.V., & Dzhardimalieva, G.I. (2026). Effect of Graphite Content on the Structural and Electrochemical Properties of MIL-88B(Fe)/Graphite Composites. *Eurasian Journal of Chemistry, 31, 3(123), 98–116.* https://doi.org/10.31489/2959-0663/3-26-5

INORGANIC CHEMISTRY

Article

Received: 20 July 2026 | Revised: 14 August 2026 |
Accepted: 19 August 2026 | Published online: 27 August 2026

UDC 546.26+544.6

https://doi.org/10.31489/2959-0663/3-26-5

Rose K. Baimuratova[1*], Ravil N. Bazargulov[1,2], Sofia A. Kleinikova[1], Ekaterina V. Zolotukhina[1], Konstantin V. Gor'kov[1], Mikhail V. Zhidkov[1], Gulzhian I. Dzhardimalieva[1,3]

[1]*Federal Research Center of Problems of Chemical Physics and Medicinal Chemistry Russian Academy of Sciences, Chernogolovka, Moscow region, Russia*
[2]*Lomonosov Moscow State University, Moscow, Russia*
[3]*Moscow Aviation Institute (National Research University), Moscow, Russia*
*(*Corresponding author's e-mail: rozab@icp.ac.ru)*

Effect of Graphite Content on the Structural and Electrochemical Properties of MIL-88B(Fe)/Graphite Composites

MIL-88B(Fe)/graphite composites are promising conductive materials for electrochemistry, combining the advantages of metal-organic frameworks and carbon. A series of composites with graphite contents from 12.5 to 75 wt.% was synthesized via in situ precipitation in aqueous medium at room temperature, using a trinuclear iron(III) oxoacetate complex as an inorganic precursor. The physicochemical characteristics were investigated by X-ray diffraction, Raman spectroscopy, SEM, TGA, nitrogen adsorption–desorption analysis, and infrared spectroscopy. An inverse linear correlation was found between the graphite content and the mass loss of the MOF composite at the first decomposition stage, attributed to dehydration. With increasing graphite weight fraction, the rate of mass loss of the composite decreases. The specific surface area nonlinearly decreases with increasing graphite content from 220 m^2/g for pristine MIL-88B(Fe) to 15.2 m^2/g for the composite with 75 wt.% graphite, while the calculated QSDFT pore diameter shifts from 4.6 nm for pure MIL-88B(Fe) to a stable 3.1 nm for the composites, indicating that graphite localizes on the outer crystal surfaces rather than penetrating the MOF pores. Electrocatalytic activity of MIL-88B(Fe) toward glucose oxidation was demonstrated by cyclic voltammetry. The results provide a physicochemical foundation for the development of electrode materials for non-enzymatic electrochemical glucose sensors based on MIL-88B(Fe) systems.

Keywords: MIL-88B(Fe), metal-organic frameworks, graphite composites, electrocatalytic activity, glucose, electrochemical sensors, in situ synthesis, porous structure

Introduction

Electrocatalysis, which accelerates electrochemical reactions at the electrode–electrolyte interface using catalysts, is widely employed in hydrogen energy applications, including fuel cells and water electrolysis systems [1–23], electrochemical energy storage devices such as batteries and supercapacitors [3], CO_2 conversion into valuable products like formate and methanol, N_2 reduction to ammonia [4–6], electrochemical wastewater treatment methods including anodic oxidation and electro–Fenton processes [7, 8], as well as in devices for metabolite monitoring, for example, for the electrocatalytic oxidation of glucose on modified electrodes [9–11]. The efficiency of electrocatalysis depends on the electrode material, which must combine high catalytic activity, good electrical conductivity, and stability under anodic polarization conditions [7].

Metal–organic frameworks (MOFs) are a class of porous coordination polymers constructed from metal ions or clusters connected by organic linkers into two- or three-dimensional structures [12]. Among iron-containing MOFs (Fe-MOFs), MIL-88B(Fe) is particularly noteworthy, as its structure consists of trimeric

iron oxo-clusters bridged by terephthalate ligands, forming a hexagonal framework with one-dimensional channels approximately 6–9 Å in diameter [13, 14].Owing to their developed porosity, which ensures efficient mass transport of reagents to the electrode surface, and the presence of catalytically active Fe^{3+}/Fe^{2+} centers capable of reversibly participating in redox reactions under an applied potential, iron-based MOFs are being actively explored for electrochemical applications [15]. MOFs can be used as electrode materials in batteries, serve as electrocatalysts for reactions occurring in fuel cells or electrolyzers, and also act as a basis for supercapacitor electrodes [16]. In contrast to non-porous metal nanoparticles or microparticles, where only surface atoms in contact with the electrolyte can be electrochemically active and reactions occur solely at the surface, in porous electrochemically active MOFs the utilization of metal ions can theoretically reach 100 % [16]. Ionic conductivity can be provided by the MOF itself, by the electrolyte, or by guest molecules introduced into the pores of the framework [17]. MIL-88B(Fe) belongs to the class of flexible metal-organic frameworks, which can reversibly change the unit cell volume upon adsorption/desorption of guest molecules. For the MIL-88 family, which is known for its "breathing" behavior, the volume change can reach 85–230 % depending on the nature of the linker and the type of guest molecules, while the crystal structure remains intact [18–20]. Pore tunability enables host-guest molecular recognition, which enhances the activity and selectivity of sorption, separation, and catalysis [21], and also makes these materials promising for electrochemical sensors. However, pristine MOFs suffer from low electrical conductivity, which limits their use as electrode materials [14]. A solution to this problem is the fabrication of MOF composites with complex architectures by combining them with carbon-based materials (activated carbon, carbon nanotubes (CNTs), fullerene, graphite, graphene oxide, etc.), as well as with nanoparticles or oxides of metals and non-metals [22–24]. The formation of MOF composites with graphite, carbon nanotubes, acetylene black, or reduced graphene oxide (rGO) enables the creation of a conductive network that improves electron transport from the external circuit to the catalytic centers of the MOF [25, 26]. In such systems, the carbon component not only enhances the overall conductivity but also acts as a dispersing support, preventing aggregation of MOF nanoparticles and increasing the number of available active sites, which in turn improves the electrochemical performance [27, 28] or photocatalytic activity [29]. Zhang et al. demonstrated that MIL-53(Fe)@rGO delivers a capacity of 550 $mA \cdot h\ g^{-1}$ after 100 cycles at 100 $mA \cdot h\ g^{-1}$ in lithium-ion batteries [27]. Jin et al. obtained a Fe_3O_4/C nanocomposite via post-synthetic thermal treatment of MIL-88B(Fe) at 600 °C, with the capacity increasing up to the 200th cycle (from ~800 to 928 $mA \cdot h\ g^{-1}$), which the authors attributed to an "activation process" [28]. It was shown that oxygen-functionalized CNTs reduce Fe(III) to Fe(II) and consequently increase the Fenton-like activity in the CNT@MIL-88B-Fe composite [29]. The potential of such composites in biosensors was demonstrated by Qin et al., who used a MIL-88A@NiFe-PB heterostructure with high sensitivity (1963.2 $\mu A \cdot mM^{-1}\ cm^{-2}$) for glucose detection [30].

However, most studies are based on the use of expensive carbon components (rGO, CNTs) and, as a rule, are limited to a single MOF/carbon ratio. Systematic data on the effect of graphite content on the structure and properties of MIL-88B(Fe)/graphite composites are lacking in the literature. In this regard, in the present work we investigated the effect of graphite content on the structure and physicochemical properties of MIL-88B(Fe)/graphite composites synthesized by in situ precipitation in aqueous medium. It was shown that varying the graphite weight fraction enables control not only of the conductivity but also of the specific surface area, morphology, and thermal stability, while preserving the porous structure of the MOF. For the first time, it is demonstrated that MIL-88B(Fe) exhibits electrocatalytic activity toward glucose oxidation, opening prospects for its use in non-enzymatic electrochemical sensors.

Experimental

Reagents and Materials

Iron(III) chloride hexahydrate ($FeCl_3 \cdot 6H_2O$, chemically pure), sodium acetate trihydrate ($CH_3COONa \cdot 3H_2O$, analytical grade), D-glucose (>99 %, $C_6H_{12}O_6$), cetyltrimethylammonium bromide (CTAB, $C_{19}H_{42}BrN$, analytical grade), potassium hydroxide (KOH, RusKhim, ≥90 %, analytical grade), and ethyl alcohol (95 %, pharmaceutical grade) were purchased from Ruskhim Trade Company and used without further purification. Terephthalic acid (1,4-benzenedicarboxylic acid, H_2BDC, 98 %) was supplied by Sigma-Aldrich. Fine graphite powder of grade GK-1, which according to GOST 17022-81 is intended for the production of drawing and office pencil leads (≥99.5 % of particles ≤63 μm), was used as the carbon component.

Synthesis of the inorganic precursor $[Fe_3O(OAc)_6]Cl$

The metal-organic framework MIL-88B(Fe) was obtained at room temperature according to a previously reported procedure [31]. As an inorganic precursor, the trinuclear iron(III) oxo-acetate complex $Fe_3(\mu_3\text{-}O)(CH_3COO)_6(H_2O)_3]Cl{\cdot}12H_2O$ ($[Fe_3O(OAc)_6]Cl$), was synthesized according to reaction (1) [32]:

$$3FeCl_3 + 6CH_3COONa + 4H_2O \rightarrow [Fe_3(\mu_3\text{-}O)(CH_3COO)_6(H_2O)_3]Cl + 6NaCl + 2HCl \quad (1)$$

A sample of $FeCl_3{\cdot}6H_2O$ weighing 56 g (0.21 mol) was dissolved in 70 mL of hot distilled water (55 °C) under stirring until complete dissolution. Sodium acetate trihydrate weighing 56.5 g (0.41 mol) was dissolved in 70 mL of hot distilled water (55 °C). After complete dissolution of both reagents, the iron(III) chloride solution was added dropwise to the sodium acetate solution, and the reaction mixture was thermostated at 55 °C and stirred for 120 min. After the stirring was completed, the solution was left for slow crystallization in air at room temperature for 12 h, and then kept for several additional days. The resulting orange-red crystalline precipitate was collected by filtration on a Büchner funnel, washed with a small amount of cold ethanol to remove impurities, and dried in an oven at 50 °C to constant weight. Calculated for $Fe_3(\mu_3\text{-}O)(CH_3COO)_6(H_2O)_3]Cl{\cdot}12H_2O$ (wt. %): C, 17.1; H, 5.6; Fe, 19.8; Cl, 4.2. Found (wt. %): C, 17.1±0.1; H, 5.70±0.15. IR spectroscopy (KBr, ν_{max}/cm^{-1}): 3523 ν(O–H); 2929 ν(C–H); 1601 $\nu_{as}(COO^-)$, 1520 $\nu_{as}(COO^-)$, 1444 $\nu_s(COO^-)$; 665 ν(Fe–O).

Synthesis of MIL-88B(Fe)/graphite composites

A series of MIL-88B(Fe)/graphite composites with varying graphite content was prepared by reacting the inorganic precursor $[Fe_3O(OAc)_6]Cl$ with the potassium salt of terephthalic acid under mechanical stirring (1000 rpm). Precursor masses and product yields are listed in Table 1.

Table 1

Precursor masses and yields for MIL-88B(Fe)/graphite composite synthesis

Sample	Graphite content, wt. %	m(graphite), g	m(KOH), g	m(H_2BDC), g	m($[Fe_3O(OAc)_6]Cl$), g	m(composite), g (yield %)
MIL-88B(Fe)	0	0	2.36	3.15	4.65	4.1 (91.1 %)
MIL-88B/graphite (75 wt %)	75	1.50	2.36	3.15	4.65	5.4 (90.1 %)
MIL-88B/graphite (50 wt %)	50	3.00	1.58	2.10	3.10	5.4 (90.1 %)
MIL-88B/graphite (25 wt %)	25	4.50	0.79	1.05	1.55	5.5 (92.0 %)
MIL-88B/graphite (12.5 wt %)	12.5	0.75	2.76	3.67	5.43	5.1 (84.7 %)

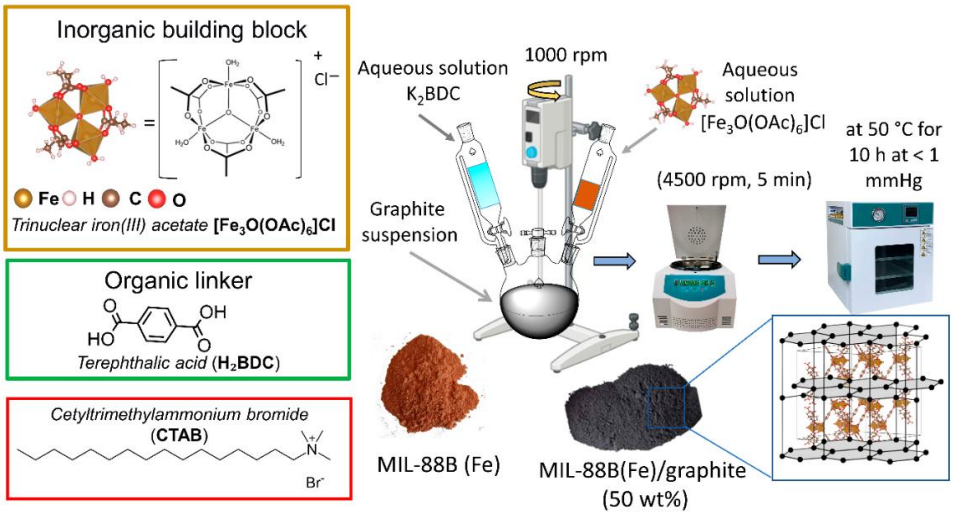

Figure 1. Schematic representation of MIL-88B(Fe)/graphite composite synthesis using the trinuclear iron(III) oxo-acetate complex

The synthesis was carried out in a 1 L three-neck round-bottom flask equipped with a mechanical overhead blade stirrer at 1000 rpm. Graphite and CTAB were first dispersed in 100 mL of water using a mechanical stirrer at 1500 rpm for 30 min at room temperature. H_2BDC was dissolved in 250 mL of water by adding

the appropriate amount of KOH. $[Fe_3O(OAc)_6]Cl$ was dissolved in 250 mL of water with heating (50–55 °C) and stirring at 250 rpm. The resulting precursor solutions were transferred to addition funnels and added dropwise to the graphite suspension over 30 min under vigorous stirring, as shown in Figure 1. The reaction mixture was stirred for 60 min at 1000 rpm. The resulting precipitate was separated by centrifugation (4500 rpm, 5 min), washed twice with water (50 mL) and ethanol (20 mL) to remove unreacted components, and dried at 50 °C in a vacuum oven for 10 h. The yields ranged from 84 to 92 % of the theoretical values (Table 1).

Characterization Methods

Carbon (C), hydrogen (H), and nitrogen (N) mass fractions in the synthesized samples were determined by combustion analysis using a Velp EMA 502 elemental analyzer (VELP Scientifica, Italy). FTIR spectra were recorded on a Bruker ALPHA spectrometer (Bruker Optik GmbH, Germany) in the range of 360–4500 cm^{-1} with a resolution of 2 cm^{-1} using KBr pellets containing 0.7 wt. % of the sample powder (32 scans). X-ray powder diffraction (XRD) patterns were collected on an Aeris Benchtop diffractometer (Malvern Panalytical, Netherlands) in Bragg–Brentano geometry with a vertical θ–θ goniometer (CuKα radiation, λ = 1.5460 Å; 2θ = 5–65°, step 0.012°). Thermogravimetric analysis (TGA) was performed on a TGA/SDTA851e thermoanalyzer (Mettler Toledo, Switzerland) in dynamic mode over 25–600 °C at a heating rate of 10 °C/min under a nitrogen atmosphere (absolute instrumental temperature accuracy ±0.5 °C, sample mass 4–6 mg, Al_2O_3 crucibles). The specific surface area, average pore radius, and pore size distribution were determined by low-temperature N_2 adsorption–desorption at 77 K on an AUTOSORB-1 analyzer (Quantachrome Instruments, USA). Samples were degassed at 120 °C for 2 h under vacuum (residual pressure $\leq 10^{-3}$ mbar) before measurement. The measurement was performed by the static volumetric method using helium for dead-volume calibration. Textural analysis and pore size distributions were evaluated using Quenched Solid Density Functional Theory (QSDFT, carbon slit-pore equilibrium model) and the t-plot method, while the Barrett–Joyner–Halenda (BJH) model was applied to characterize the general mesoporous features. Isotherm types were classified according to IUPAC 2015 recommendations. The morphology of the samples was examined by scanning electron microscopy (SEM) using an EM−30 microscope (Coxem, South Korea) at an accelerating voltage of 15 kV in secondary electron (SE) detection mode. Raman spectroscopy was performed using a Confotec® NR500 scanning confocal Raman microscope (SOL instruments, Belarus) equipped with a green laser (532 nm). The laser power of ~1.3 mW was chosen to avoid thermal degradation of the MOF. The signal accumulation time was 60 s. Spectra were recorded in the range of 100–1700 cm^{-1}, which covers the characteristic vibrational modes of both the graphite matrix and the MOF. The morphology and distribution of MOF particles within the graphite matrix were studied using an Optelics Hybrid confocal laser microscope (Lasertec Corp., Japan) equipped with planar apochromatic objectives (50× and 100× magnification).Quantitative particle size analysis was performed using ImageJ software [33] from bright-field optical micrographs.

Electrochemical Measurements

Electrochemical measurements were carried out using an Autolab PGSTAT 101 potentiostat (Metrohm-Autolab, Netherlands) and screen-printed three-electrode (SPE) test strips (Elta Ltd., Zelenograd, Russia). The three-electrode system comprised a graphite counter electrode, a custom Ag/AgCl reference electrode, and a graphite working electrode modified with a MOF or a composite. The reference electrode was prepared by electrooxidizing silver in 1 M NaCl at 1.6 V for 20 s. The potential of the resulting Ag/AgCl, Cl^- electrode in 0.15 M NaCl was 0.278 V vs. the standard hydrogen electrode (SHE). All potentials herein are given vs. this reference electrode. The working electrode was modified by applying a drop of a suspension of the studied MOF in 0.1 M acetate buffer (pH 5.5). For the electrochemical studies, a 100 μL aliquot of a solution was applied onto the test strip. Cyclic voltammograms were recorded at a scan rate of 0.02 V/s. Chronoamperometric data were recorded at an applied constant potential of 0.5 V.

Results and Discussion

Synthesis of MIL-88B(Fe)/Graphite Composites

The MIL-88B(Fe)/graphite composites were synthesized by in situ precipitation of the MOF onto graphite surfaces in an aqueous medium at room temperature to nucleate and grow directly on the graphite surface, ensuring intimate interfacial MOF–graphite contact and, consequently, efficient electron transport between the two components. The advantages of the proposed method over known approaches are: (i) use of a trinuclear acetate precursor with defined coordination geometry instead of $FeCl_3$ enables targeted formation

of the framework structure with the required network topology, implementing a "rational design" strategy [31, 34]; (ii) the aqueous medium eliminates the use of toxic dimethylformamide (DMF), traditionally employed in MIL-88B(Fe) synthesis [13]; and (iii) room temperature reduces energy consumption and simplifies scale-up. To improve the wettability of the graphite surface with water, prevent sedimentation of graphite particles, and ensure uniform distribution of graphite throughout the composite volume, cetyltrimethylammonium bromide (CTAB), a cationic surfactant, was introduced into the reaction mixture during the synthesis. It is known that the addition of CTAB reduces the interfacial tension at the graphite–water interface [35], which prevents aggregation of hydrophobic particles and allows a homogeneous suspension to be obtained, which is necessary for uniform MOF deposition onto the graphite surface.

Elemental Composition

CHNO elemental analysis results for individual components and synthesized samples are presented in Table 2. The actual graphite content in each sample was calculated from elemental analysis, noting that the total carbon content in the composite ($C_{composite}$) equals the sum of contributions from graphite and from the MOF:

$$C_{\text{composite}} = x \cdot C_{\text{graphite}} + (1 - x) \cdot C_{\text{MOF}} \quad (2),$$

where x is the graphite mass fraction; $(1 - x)$ is the MIL-88B(Fe) mass fraction. Therefore:

$$x = \frac{C_{composite} - C_{MOF}}{C_{graphite} - C_{MOF}} \times 100\% \quad (3)$$

where $C_{composite}$, C_{MOF}, and $C_{graphite}$ are the carbon contents in the composite, in MIL-88B(Fe), and in pristine graphite, respectively, determined by CHNO elemental analysis.

Table 2

Elemental analysis results of MIL-88B(Fe)/graphite composites

Sample	C, wt %	H, wt %	O, wt %	Graphite content, wt %
Graphite	98.2 ± 0.9	0.12 ± 0.05	2.47 ± 0.23	-
$[Fe_3O(OAc)_6]Cl$	17.12 ± 0.13	5.7 ± 0.2	29 ± 1	-
MIL–88B(Fe)	38.1 ± 0.3	2.6 ± 0.1	31.5 ± 0.5	0
MIL-88B(Fe)/graphite (12.5 wt %)	43.06 ± 0.91	3.1 ± 0.1	32.38 ± 0.35	8.3 ± 1.5
MIL-88B(Fe)/graphite (25 wt %)	53.30 ± 0.34	2.60 ± 0.01	28.4 ± 0.8	25.3 ± 0.7
MIL-88B(Fe)/graphite (50 wt %)	67.35 ± 0.05	1.65 ± 0.03	18.00 ± 0.24	48.7 ± 0.8
MIL-88B(Fe)/graphite(75 wt %)	84.55 ± 0.06	0.78 ± 0.21	9.5 ± 0.2	77.3 ± 0.7

As shown in Table 2, with increasing graphite fraction across the composite series, the carbon mass fraction increases progressively from 43.06 % (12.5 wt % graphite) to 84.55 % (75 wt % graphite), while the hydrogen content decreases correspondingly from 3.1 to 0.78 wt %. The oxygen content decreases monotonically from 32.38 to 9.5 wt % due to the reduced proportion of MIL-88B(Fe) in the sample. The actual graphite content calculated from CHNO data agrees well with the nominal content, with deviations of no more than 1.5 wt % for samples with 25, 50, and 75 wt % graphite. The largest relative deviation is observed for the 12.5 wt % graphite sample, likely due to adsorption of residual solvent (water).

X-Ray Powder Diffraction

The XRD patterns of the synthesized MIL-88B(Fe)/graphite composites (Figure 2) show an intense reflection at $2\theta \approx 26.5°$, corresponding to the (002) reflection of the hexagonal layered graphite structure (JCPDS 75-1621, d002 = 3.354 Å). Weak reflections at 17.4 °, 25.2°, and 28.0° are attributable to terephthalic acid (CCDC 1269122). Formation of this impurity phase is associated with the low aqueous solubility of terephthalic acid [36, 37] and the high rate of acetate-group substitution. As a result, a portion of the ligand is protonated in the acidic medium and does not have sufficient time to be fully incorporated into the framework. It is known that due to the high reaction rates and steric hindrance, acetate groups may not be completely substituted, leading to the formation of defective linkers [38, 39] in the resulting MOF structure. These defective linkers can coordinate to the metal cluster via only one carboxylate group, with the other group protruding into the pore cavity. This favors the retention of organic molecules inside the framework and results in the inclusion of terephthalic acid within the MOF pores, from which it is difficult to remove

even after repeated washing during the synthesis [40–42]. The absence of characteristic MIL-88B(Fe) reflections when water is used as the solvent is related to the reversible contraction of the crystal lattice, referred to as "breathing" [19, 43, 44], which is caused by the formation of hydrogen bonds between the metal-organic framework and guest molecules [45]. To confirm the flexibility of the synthesized MIL-88B(Fe), additional XRD studies were performed. The sample obtained after synthesis in aqueous solution and drying exhibits a diffraction pattern with a broadened signal in the low-angle region ($2\theta < 6.5°$), which does not allow unambiguous identification of the crystalline reflections characteristic of MIL-88B(Fe). This broadening is attributed to the transition of the framework to the closed (dry) form, which is characterized by anisotropic broadening of the (hk0) reflections, up to their complete disappearance, due to disordering in the (ab) plane caused by the removal of guest molecules and a decrease in the a parameter [18]. After soaking the same sample in DMF for 24 h, intense reflections appear at $2\theta \approx 7.12°$ and 8.75° ($d \approx 12.5$ Å and 10.1 Å, respectively), corresponding to a transition to the expanded (open) phase stabilized by DMF molecules and restoration of long-range crystalline order. This observation is consistent with previously reported rotation of metal clusters and phenyl rings around the O–O axis of carboxylate groups (a "knee-type" rotation axis) upon exposure to water molecules in MIL-88B(Fe) [46]. Similar behavior has been reported for MIL−88B(Fe)/Fe_3S_4 composites [47], MIL-88B(Fe)/nanorods [48], and Fe_3O_4/MIL-88B(Fe) [32].

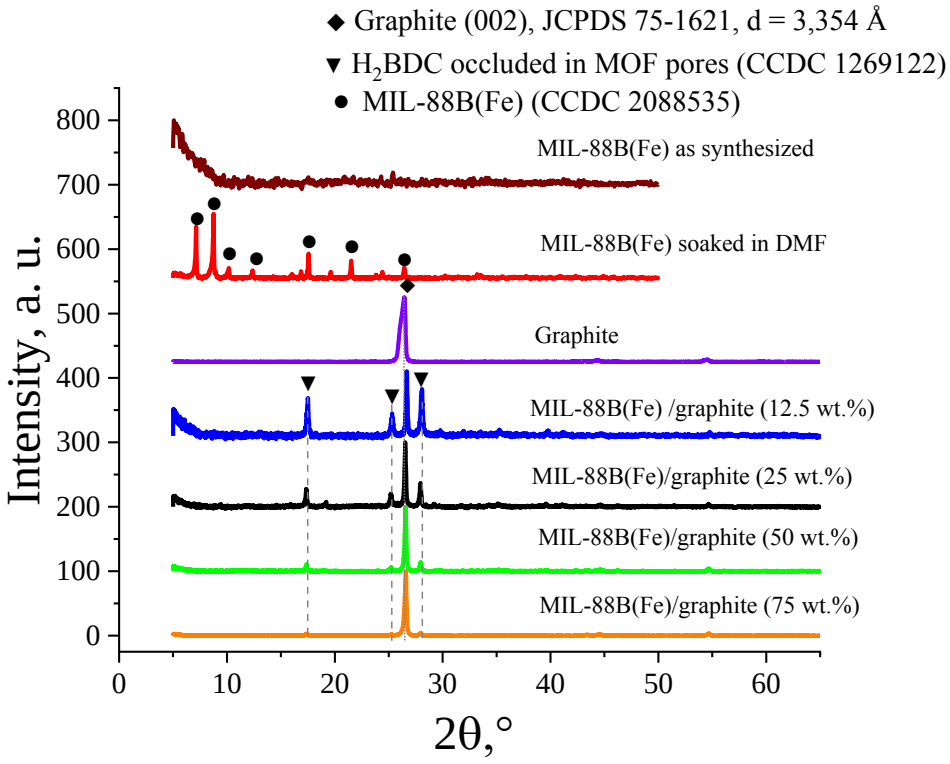

Figure 2. X-ray diffraction patterns of MIL-88B(Fe) and synthesized composites (CuKα, λ = 1.5460 Å)

Infrared Spectroscopy

FTIR spectra of MIL-88B(Fe) and MIL-88B(Fe)/graphite composites with various graphite contents are shown in Figure 3.

The FTIR spectra of the synthesized samples exhibit characteristic bands confirming the formation of MIL-88B(Fe). The symmetric and asymmetric stretching vibrations of the carboxylate groups are observed at 1424 and 1575 cm^{-1}, respectively; the ν(C=C) band of the aromatic ring appears at 1510 cm^{-1}, while the ν(C–O) and ν(C–C) stretching modes are detected at 1287 cm^{-1}. With increasing graphite content, the intensities of all MIL-88B(Fe) bands decrease progressively. Broadening and splitting of both asymmetric and symmetric carboxylate stretching bands is also observed. This splitting indicates the formation of inequivalent COO^- coordination modes in the composites, likely caused by the influence of the graphite surface in proximity to the carboxylate fragments of the metal-organic framework. The presence of a band at 1688 cm^{-1}, assigned to ν(C=O) of free carboxylic groups, indicates the presence of defective (dangling) link-

ers coordinated to the metal cluster through only one carboxylate group [49]. The bands at 668 and 528 cm^{-1} are characteristic of Fe–O stretching vibrations and Fe–O–Fe bridging modes [50], confirming the retention of the trimeric oxoacetate cluster. A broad band in the range of 3200–3600 cm^{-1} with a maximum at 3435 cm^{-1}, whose intensity increases with rising MIL-88B(Fe) content, is attributed to O–H stretching vibrations of hydroxyl groups involved in intermolecular hydrogen bonding [50].

The spectrum of MIL-88B(Fe) displays all characteristic bands of an iron-based carboxylate MOF [50,51]. Intense bands at 1546 and 1387 cm^{-1} correspond to the asymmetric and symmetric stretching vibrations of the carboxylate groups coordinated to the Fe_3O clusters. The absorption band at 725 cm^{-1} is assigned to the C–H bending (out-of-plane) vibrations of the disubstituted aromatic ring. The presence of the aromatic moiety is further confirmed by the band at 3060 cm^{-1}, attributed to the =C–H stretching vibrations [52]. In the spectrum of H_2BDC, the most intense bands are observed at 725, 878, and 779 cm^{-1}, characteristic of out-of-plane C–H deformation modes in the 1,4-disubstituted benzene ring, along with the ν(C=O) band of the free carboxyl group at 1671 cm^{-1} [51, 52]. The frequency difference between the asymmetric and symmetric carboxylate stretching vibrations ($\Delta\nu = \nu_{as} - \nu_{sym} \approx 151–159\ cm^{-1}$) is indicative of a bidentate bridging coordination mode of the carboxylate ions [53] and is in full agreement with literature data for MIL-88B(Fe).

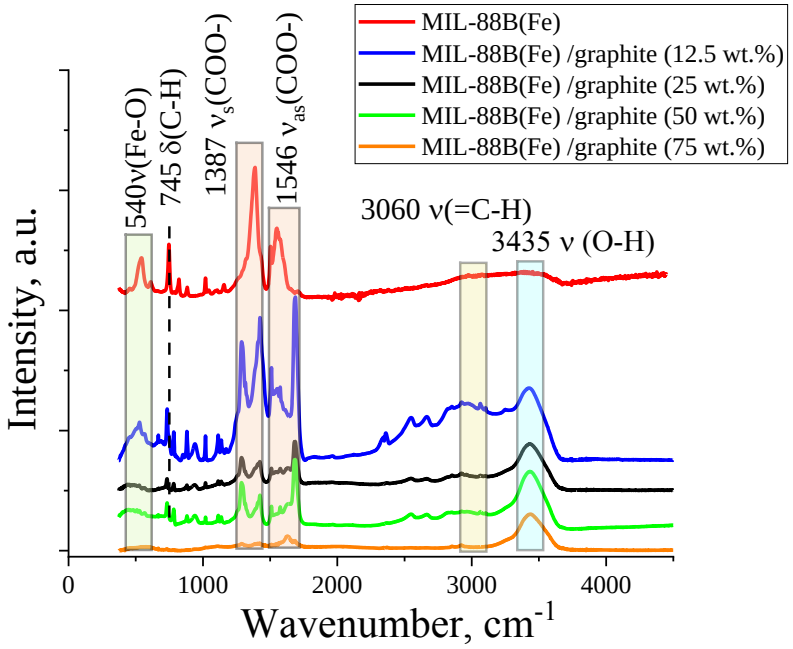

Figure 3. FTIR spectra of MIL-88B(Fe) and MIL-88B(Fe)/graphite composites (KBr pellets, 0.7 wt %)

Raman Spectroscopy

Raman spectroscopy was performed for additional phase identification and assessment of the structural features of the MIL-88B(Fe)/graphite composites (Figure 4). The spectra are presented in the range of 1000–1700 cm^{-1}, covering the characteristic vibrational modes of the graphite and the organic linker of the MOF. As seen in Figure 4a, the pristine graphite shows a D band at ~1350 cm^{-1}, assigned to the A_{1g}-symmetric vibration of defective sp^2-carbon sites, which becomes Raman-active only upon symmetry breaking through a double-resonance process [54]. To assess the degree of disorder and crystallite size, the I_D/I_G ratio is commonly used, where I_G is the intensity of the G peak at ~1580 cm^{-1}, corresponding to the C–C stretching vibrations in an ideal plane [54, 55]. The integrated area ratio of the corresponding graphite peaks was 0.255, indicating a low concentration of structural defects [54, 55]. Using the Tuinstra–Koenig equation applied to the peak height ratio (~0.162), the calculated crystallite size of graphite was 27 nm, which is characteristic of nanocrystalline graphite with low defect density [54]. For the composite with 12.5 wt % graphite, an increase in the integrated intensity ratio of the corresponding graphite peaks (~0.41) is observed, indicating an increase in the defect concentration in graphite during the synthesis of the composite. For samples with higher graphite content (25, 50, and 75 wt %), significant overlap of the D and G bands of graphite with the bands of the aromatic linker of MIL-88B(Fe) is observed. Nevertheless, qualitative analysis of the Raman spectra

indicates that the graphite structure is preserved in the composites, while the observed changes in the defect density suggest an interfacial interaction between graphite and the MOF, likely of a physical nature.

In the Raman spectra of both pristine MIL-88B(Fe) and the MIL-88B(Fe)/graphite (12.5 wt %) composite, characteristic bands of the terephthalate linker are observed. The band in the region of 1600–1615 cm^{-1} has been assigned by some authors to the asymmetric stretching vibrations of the carboxylate group, $\nu_{as}(COO^-)$ [56, 57], while others attribute it to the C=C stretching vibrations of the benzene ring [25, 58]. In the literature, the symmetric carboxylate stretching vibrations $\nu_s(COO^-)$ of MIL-88B(Fe) appear in the Raman spectrum at ~1455 cm^{-1}, whereas the broad absorption in the range of 1300–1430 cm^{-1} is assigned to the C–C and C–O vibrations of the aromatic ring of the terephthalate linker [56, 57]. In the present study, a shift of the carboxylate stretching band to lower wavenumbers (~1427 cm^{-1}) is observed, likely due to formation of partially substituted structures upon interaction with graphite, consistent with FTIR data. Upon the introduction of graphite, the intensity of these bands initially increases (12.5 wt % graphite) and then decreases due to the shielding effect and the reduced MOF fraction in the composite, which correlates with the FTIR results. The band in the range of 1132–1138 cm^{-1} is attributed to the C–C bond vibrations between the benzene ring and the carboxylate group [56].

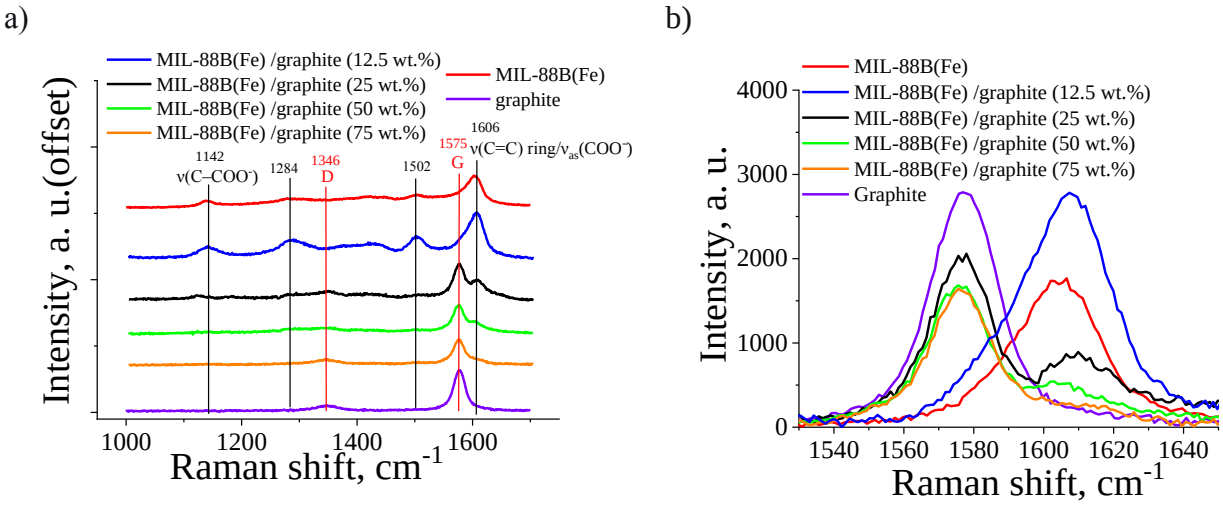

Figure 4. Raman spectra of graphite, MIL-88B(Fe), and MIL-88B(Fe)/graphite composites with various graphite contents (a), and a fragment of the Raman spectra in the range of 1540–1640 cm^{-1} showing the overlap of the graphite G peak and the MIL-88B(Fe) bands (b)

In Raman spectroscopy, the intensity of a band is proportional to the square of the derivative of polarizability with respect to the normal coordinate of the vibration. For low-frequency modes, such as Fe–O stretching vibrations and out-of-plane C–H bending vibrations of the aromatic ring (γ(C–H)), the change in polarizability during vibration is relatively small. Consequently, these modes exhibit a small Raman scattering cross-section and produce weak signals (Figure S1), especially against the background of the intense D and G bands of graphite, which possess high scattering cross-sections.

Specific Surface Area and Pore Size Analysis

Results of low-temperature nitrogen adsorption are summarized in Table 3. Pristine MIL-88B(Fe) exhibits a Type IV nitrogen adsorption–desorption isotherm according to the IUPAC classification, with a hysteresis loop (Figure 5), indicative of capillary condensation in mesopores, with a high specific surface area (S_{BET} = 220 m^2/g) and an average pore diameter of 3.6 nm. The specific surface area of MIL-88B(Fe) is comparable to literature data for MIL-88B(Fe), which range from 15 to 428 m^2/g depending on the synthesis and activation conditions [59–61].

Table 3

Specific surface area (S_{BET}), pore volume (V_{BJH} and V_{QSDFT}) and average pore diameter (d_{BJH} and d_{QSDFT}) of MIL-88B(Fe)/graphite composites

Sample	S_{BET}, m^2/g	V^*_{total}, cm^3/g *(p/p_o =0.99)	V_{BJH}, cm^3/g	d_{BJH}, nm	V_{QSDFT}, cm^3/g	d_{QSDFT}, nm
MIL–88B(Fe)[a]	220	0.32	0.25	3.6	0.25	4.6
MIL-88B(Fe)/graphite (12.5 wt %)	93	0.10	0.07	3.5	0.08	3.1
MIL-88B(Fe)/graphite (25 wt %)	48	0.06	0.05	3.5	0.05	3.1
MIL-88B(Fe)/graphite (50 wt %)	41	0.07	0.06	3.6	0.06	3.1
MIL-88B(Fe)/graphite (75 wt %)	15	0.04	0.04	3.5	0.03	3.1
Graphite	12	0.04	0.04	3.4	0.03	2.8

[a] *according to t-plot analysis V_{micro}=0.018 cm^3/g, S_{micro}=46 m^2/g, S_{ext}=174 m^2/g.*

As can be seen from Table 3, the *in situ* synthesis leads to a non-monotonic decrease in the specific surface area with increasing graphite content. For the sample with 12.5 wt % graphite, the BET-specific surface area was found to be 92.5 m^2/g, which is less than half the theoretical value for a physical mixture (194 m^2/g). The most pronounced drop in S_{BET} is observed upon increasing the graphite content from 12.5 to 25 wt % (from 92.5 to 48.2 m^2/g), which may be attributed to agglomeration of MIL-88B(Fe) particles, blockage of the MOF surface by graphite sheets, or changes in the morphology or defect formation in the MOF structure in the presence of graphite, consistent with the FTIR data. The Type IV isotherms with H3-type hysteresis reflect mesoporosity and interparticle voids, as the intrinsic micropores of flexible MIL-88B(Fe) contract upon guest removal (Figure 5a) [18–20]. The t-plot analysis shows a minor micropore volume of 0.018 cm^3/g for the MIL-88B(Fe) and zero microporosity for the composites. According to QSDFT analysis (Table 3), the pore diameter shifts from 4.6 nm for pure MIL-88B(Fe) to a stable peak maximum at 3.1 nm for all composites (Figure 5b). This consistent position indicates that the internal crystalline framework of the MOF is preserved during the *in situ* synthesis, while the graphite layers introduce a geometric constraint that governs the interstitial mesoporous space.

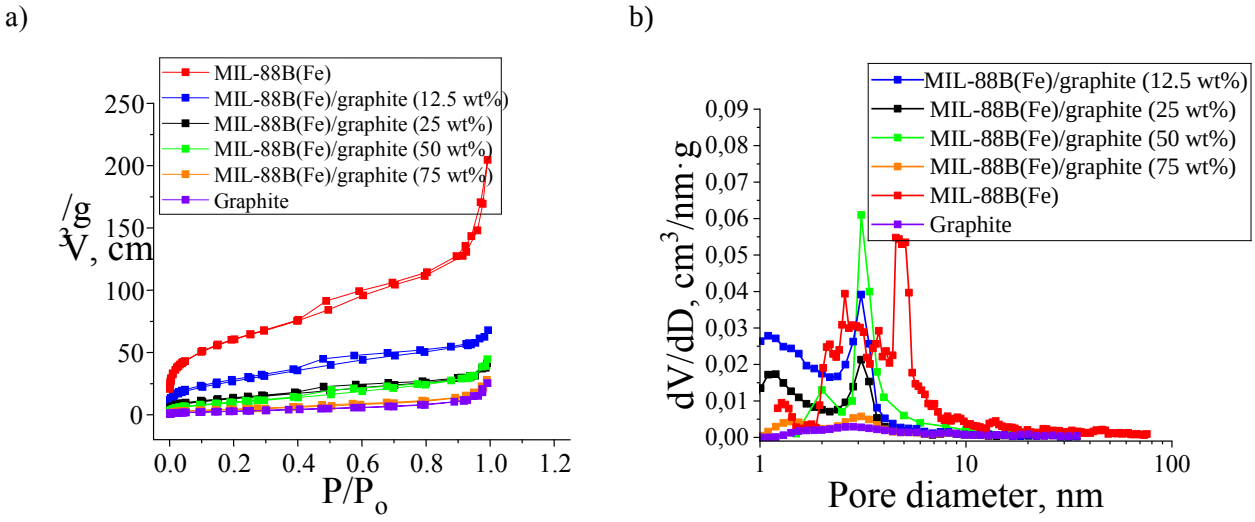

Figure 5. Nitrogen adsorption–desorption isotherms at 77 K (a) and differential pore size distribution curves for MIL-88B(Fe)/graphite composites (b)

Thermogravimetric Analysis

The thermal behavior of the samples was investigated by thermogravimetric analysis (TGA) in the range of 25–600 °C under a nitrogen atmosphere. All samples containing MIL-88B(Fe) exhibit a multistage weight loss. The data on the stages and temperature characteristics are summarized in Tables 4 and 5.

Table 4

Main stages of thermal decomposition of the MIL-88B(Fe)/graphite composites according to TGA data

Sample	Stage	Temperature range, °C	Mass loss, %
MIL–88B(Fe)	I	31-234	11.01
	II	235-372	8.19
	III	373-600	32.55
MIL-88B(Fe)/graphite (12.5 wt %)	I	31-250	6.33
	II	251-358	24.66
	III	359-600	19.13
MIL-88B(Fe)/graphite (25 wt %)	I	31-254	5.13
	II	255-355	15.97
	III	356-600	18.05
MIL-88B(Fe)/graphite (50 wt %)	I	31-264	5.44
	II	265-338	14.6
	III	339-600	19.11
MIL-88B(Fe)/graphite(75 wt %)	I	31-247	1.85
	II	248-327	4.63
	III	328-600	7.31
Graphite	I	31-600	1.95

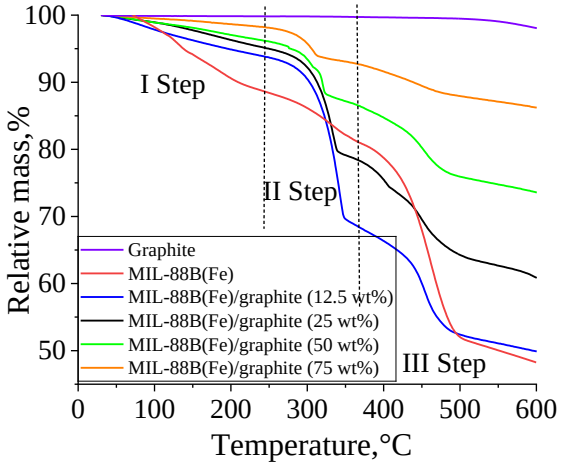

Figure 6. TGA curves of MIL-88B(Fe) and its composites, recorded at a heating rate of 10 °C/min under a nitrogen atmosphere

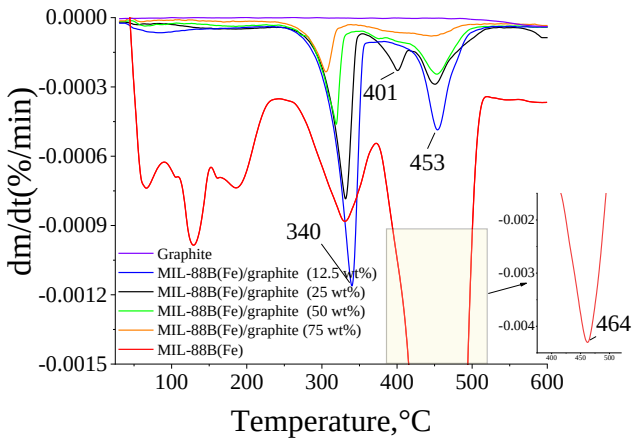

Figure 7. DTG curves of pristine MIL-88B(Fe) and its composites

Table 5

TGA data and residual mass at 600 °C (wt.%) for MIL-88B(Fe) and MIL-88B(Fe)/graphite composites

Sample	TGA data, °C						Residual mass at 600 °C, wt. %
	$T_{5\,\%}$	$T_{10\,\%}$	$T_{20\,\%}$	$T_{30\,\%}$	T_{max1}	T_{max2}	
MIL–88B(Fe)	138	209	386	444	336	464	48.3
MIL-88B(Fe)/graphite (12.5 wt %)	195	303	333	348	340	453	49.9
MIL-88B(Fe)/graphite (25 wt %)	249	313	338	447	330	401;451	60.9
MIL-88B(Fe)/graphite (50 wt %)	277	320	451	-	319	453	73.6
MIL-88B(Fe)/graphite(75 wt %)	305	439	-	-	305	446	86.2
T_i % — temperature of i % weight loss; Tmaxj — temperature of the maximum decomposition rate according to the DTG curve.							

For MIL-88B(Fe), three main decomposition stages are observed (Figure 6). The first stage (up to 234 °C, mass loss 11.0 %) corresponds to the removal of physically adsorbed and coordinated water from the framework pores. The second stage (8.2 %, 235–372 °C) is attributed to decarboxylation of the organic linker. The most significant mass loss occurs in the third stage (32.6 %, 373–600 °C) and is associated with complete decomposition of the terephthalate ligand to form Fe_2O_3 [62].

Comparison of the TGA data (Table 4) and elemental CHNO analysis (Table 2) reveals quantitative correlations between the actual graphite content and the thermal behavior of the MIL-88B/graphite composites. For all graphite-containing composites, the onset of the third decomposition stage is shifted to lower temperatures, specifically 328–359 °C, and its intensity regularly decreases with increasing graphite fraction. The mass loss in the third stage decreases from 19.13 % for the sample containing 12.5 wt. % graphite to 7.31 % for the sample with 75 wt% graphite, which is directly proportional to the decrease in the MOF content. An inverse linear correlation is observed between the graphite content and the mass loss in the first stage (30–250 °C), attributed to dehydration. For the sample with 75 % graphite, the mass loss in the first stage is only 1.85 wt. %, indicating a sharp decrease in surface hydrophilicity at high hydrophobic graphite loadings. Notably, the sample containing 8.3 % graphite, as determined by elemental analysis, shows a higher specific mass loss during the second decarboxylation stage than the pristine MOF. However, the introduction of 8 % graphite, corresponding to the MIL-88B/graphite composite with 12.5 wt. % graphite, already reduces the high-temperature loss in stage III from 32.6 % to 19.1 %, while further increasing the graphite fraction up to 50 % causes no additional decrease in mass loss. Overall, with increasing graphite weight fraction, the rate of mass loss associated with decarboxylation decreases (Figure 7).

The temperature of 5 % mass loss ($T_{5\,\%}$) increases from 138 °C for MIL-88B(Fe) to 305 °C for the MIL-88B(Fe)/graphite (75 wt. %) sample. A similar trend is observed for T10 %, which increases from 209 to 439 °C. This is due to the fact that the mass loss of pristine graphite up to 600 °C is only 1.95 %, which accounts for the increased apparent thermal stability of the composite. The residual mass at 600 °C monotonically increases from 48.25 to 86.21 %, reflecting the combined contribution of Fe_2O_3 and partially retained graphite (Table 5).

The DTG curves reveal two main maxima of the mass loss rate (T_{max1} and T_{max2}). The first maximum shifts from 131 °C for MIL-88B to 305–340 °C for the samples with 50–75 % graphite, indicating a change in the dehydration mechanism in the presence of graphite (Figure 7). The second maximum lies in the range of 446–464 °C for the entire composite series and can be attributed to the decomposition of the organic linker. For the composition with 25 % graphite, two mass loss rate maxima are observed at 401 and 451 °C, which may indicate heterogeneity of the resulting composite. For the graphite-containing samples, the residual mass includes both Fe_2O_3 from the MOF component and graphite partially retained under the experimental conditions (600 °C).

Morphology and Homogeneity of Component Distribution

In the optical micrographs (Figure 8, Figure S2), MOF particles are visualized as uniformly distributed orange inclusions against a dark background of graphite particles. Due to the color contrast between the MOF particles and the graphite matrix, automatic image segmentation with threshold-based object detection was performed. The linear particle size was calculated from the measured cross-sectional area, assuming a spindle-shaped elongated elliptical morphology with an aspect ratio of k = 2 [63] (S1). With increasing graphite content from 12.5 to 75 wt. %, the average particle length decreases from 3.05 ± 0.54 μm to 1.45 ± 0.49 μm (Figure S3). The observed decrease in particle size with increasing graphite content can be attributed to spatial confinement, where the excess graphite surface hinders further growth of MOF crystals and increases the number of nucleation sites.

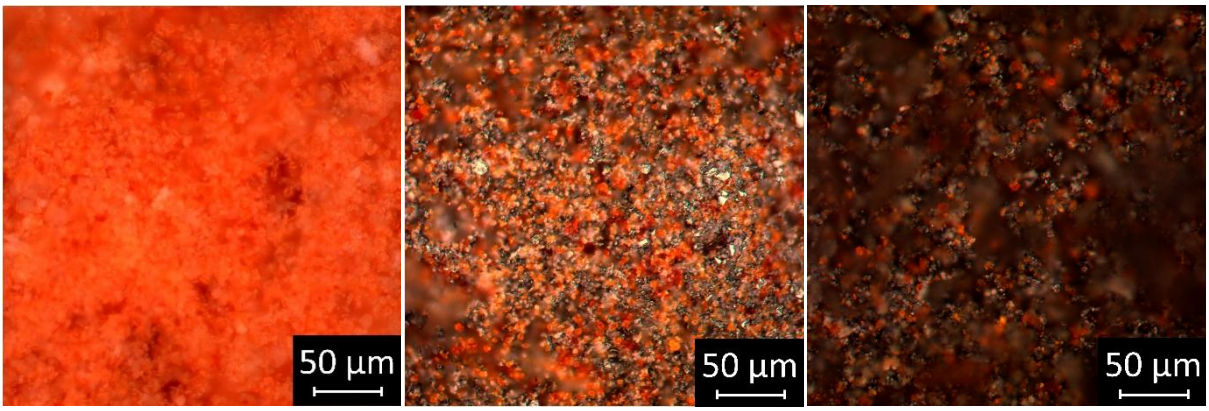

MIL-88B (Fe) | MIL-88B(Fe)/graphite (12,5 wt%) | MIL-88B(Fe)/graphite (25 wt%)

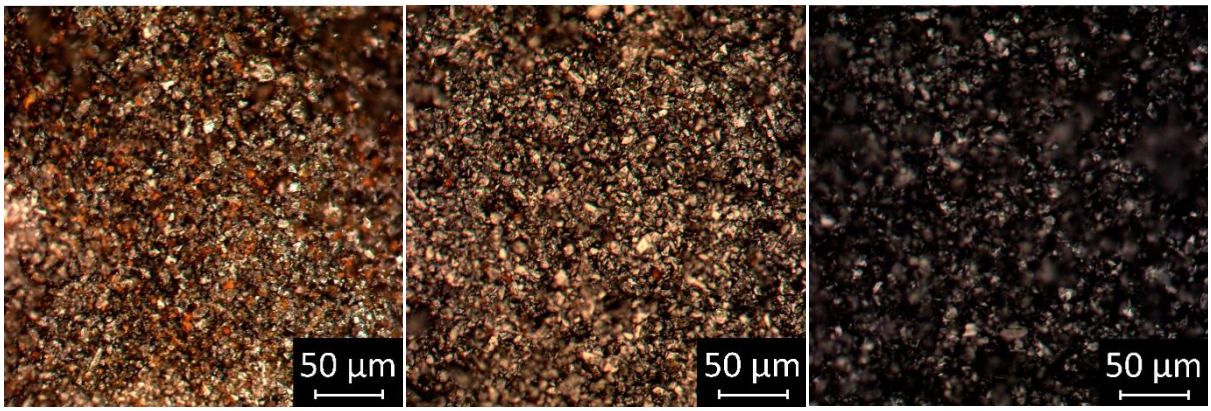

MIL-88B(Fe)/graphite (50 wt%) | MIL-88B(Fe)/graphite (75 wt%) | Graphite

Figure 8. Optical micrographs of MIL-88B(Fe)/graphite composites with different graphite contents (×50 objective, 925x magnification)

As can be seen from the SEM images (Figure 9a), MIL-88B(Fe) consists of needle-like elongated crystals with an average length of 7.27 ± 0.03 µm, whereas pristine graphite exhibits a flaky morphology (Figure 8f) with a particle size of 7.6 ± 0.2 µm and a tendency to aggregate. In the composites, even at 12.5 wt% graphite, aggregates with sharp edges are formed (Figure S4), with an average size of 12.8 ± 4.8 µm. At 25 wt% graphite, the particle size increases to 28.8 ± 8.6 µm, indicating enhanced aggregation. Further increases in graphite content to 50 and 75 wt% lead to a decrease in the average size to 9.0 ± 3.9 and 10.0 ± 2.0 µm, respectively, due to the dominance of the fine graphite phase. The observed non-monotonic particle size variation results from the balance between MOF crystal aggregation at low graphite contents and the dominance of the fine graphite phase at higher loadings.

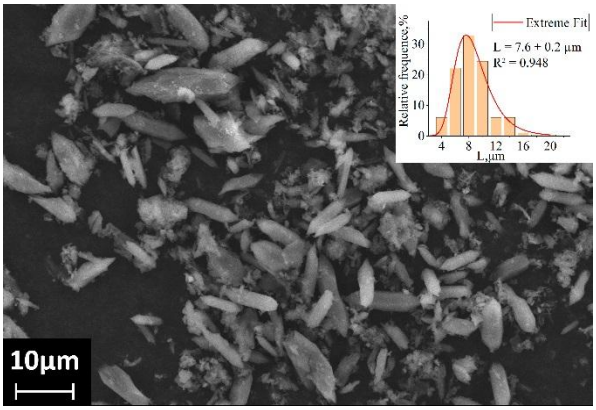

a) MIL-88B (Fe)

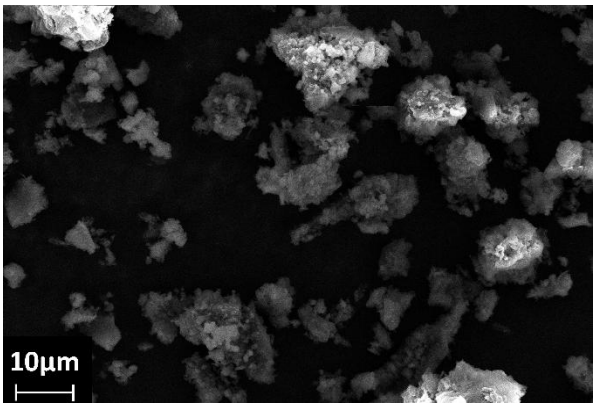

b) MIL-88B(Fe)/graphite (12,5 wt%)

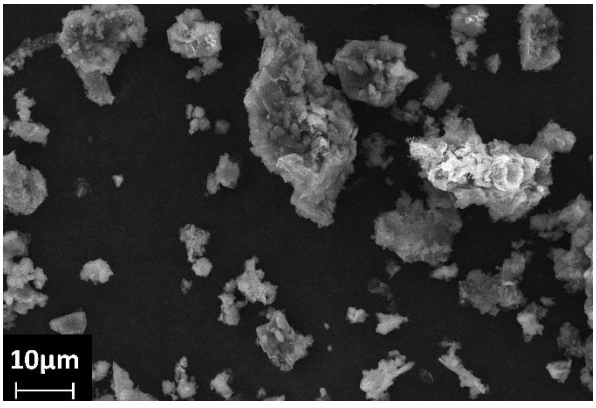

c) MIL-88B(Fe)/graphite (25 wt%)

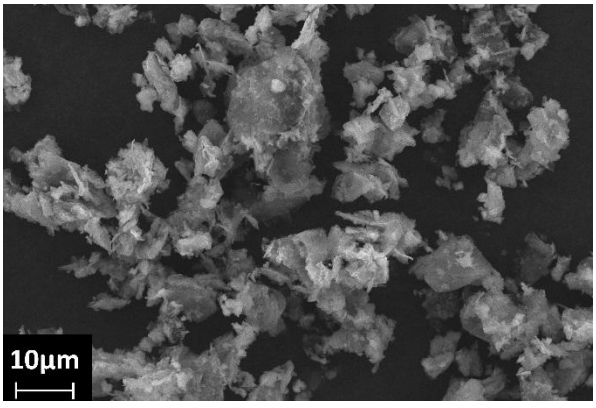

d) MIL-88B(Fe)/graphite (50 wt%)

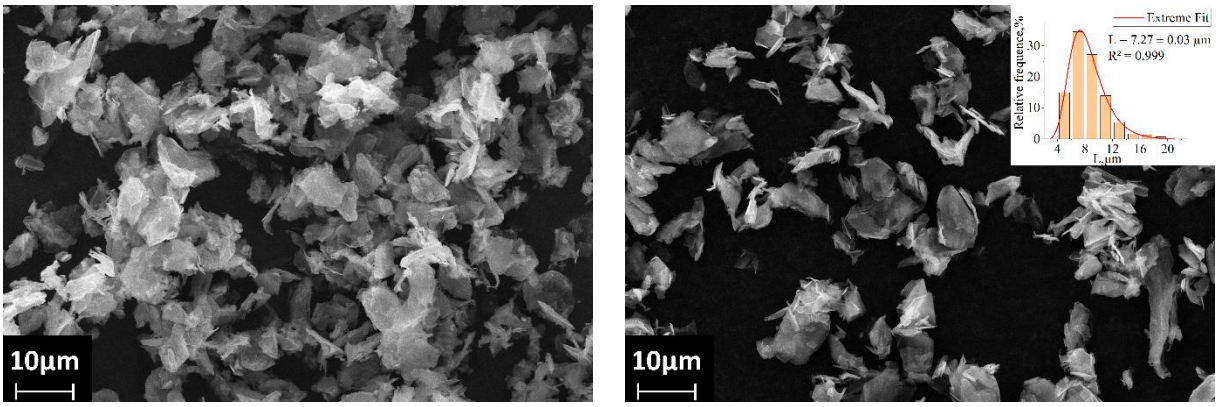

e) MIL-88B(Fe)/graphite (75 wt%) f) graphite

Figure 9. SEM images of the samples:a) MIL-88B(Fe); b) MIL-88B(Fe)/graphite (12.5 wt%); c) MIL-88B(Fe)/graphite (25 wt%); d) MIL-88B(Fe)/graphite 50 wt%); e) MIL-88B(Fe)/graphite (75 wt%); f) pristine graphite

Electrochemical Studies

The electrochemical properties of the synthesized materials were examined using cyclic voltammetry. Figure 10 shows the CV curves recorded over a wide potential range from -1.1 to 1.0 V in a 0.01 M NaOH solution. The oxygen reduction reaction region is observed at E < -0.5 V, and the oxygen evolution reaction region — at E > 0.8 V[64]. Pure MIL-88B(Fe) applied onto the working electrode exhibited low currents due to its poor electrical conductivity. An increase in the graphite content leads to an enhancement of the Faradaic currents on the CV curves (see curve for MIL-88B(Fe)/graphite (50 wt%) as a representative sample). Nevertheless, the addition of 50 wt% carbon black to pure MIL-88B(Fe) to improve the conductivity of the active layer leads to higher capacitive currents in the 0–0.4 V region compared to the MIL-88B(Fe)/graphite composite, despite their identical carbon content and mass loading. This observation indicates a smaller specific surface area for the graphite-based composite, which correlates with the BET data (Table 3). Moreover, the redox reactions within the carbon black-containing layer initiated at lower overpotentials compared to those for the graphite-containing composite.

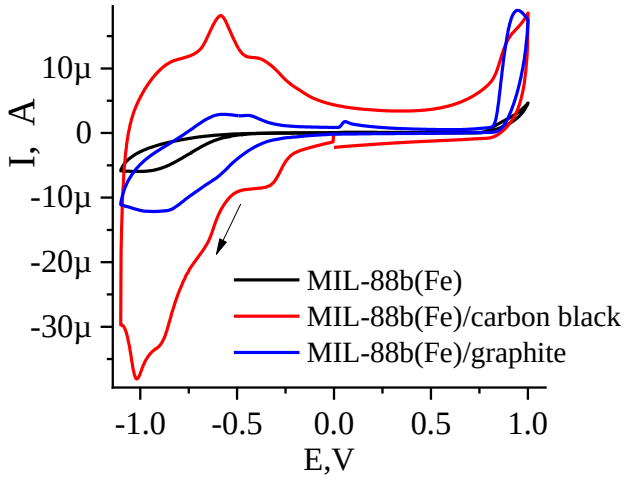

Figure 10. Cyclic voltammograms (scan rate 0.02 V/s) for the test strips with a graphite working electrode modified with MIL-88B(Fe), MIL-88B(Fe)/carbon black and MIL-88B(Fe)/graphite (50 wt%) composite in 0.01 M NaOH + 0.15 M NaCl.

Among the studied conditions, electrocatalytic activity toward glucose oxidation was observed exclusively for the MIL-88B(Fe)/carbon black in the alkaline medium (0.01 M NaOH), whereas this material remained inactive in acidic and neutral electrolytes. The use of the MIL-88B(Fe)/carbon black composition for electroanalytical testing is a rational way to avoid increasing the MOF content in the active layer, which

would otherwise lead to an increase in its thickness and ohmic resistance. As seen from the CV curves (Fig. 11a), an electrooxidation wave appears at E > 0.4 V in the presence of glucose. The chronoamperometric curves were recorded at an applied potential of 0.5 V (Fig. 11b). The steady-state currents increased with glucose concentration up to 5 mM, whereas higher concentrations did not lead to a further rise in current. The linear detection range (LDR), for the SPE modified with the MIL-88B(Fe)/carbon black composition, estimated from current values at 5 s, was 0.5...5 mM of glucose (R^2 = 0.9531). The sensitivity calculated from the linear regression in the LDR was 23 μA mM^{-1} cm^{-2}, the glucose detection limit was 0.17 mM.

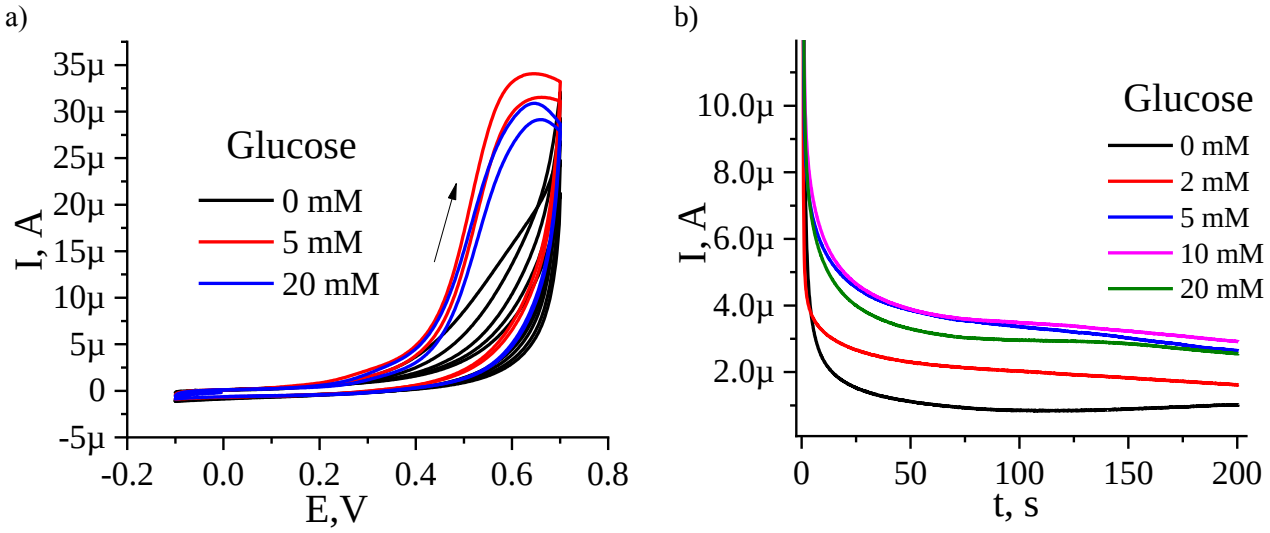

Figure 11. Cyclic voltammograms (scan rate 0.02 V/s) (a) and chronoamperometric curves recorded at 0.5 V (b) for test strips with a graphite working electrode modified with the MIL-88B(Fe)/carbon black in 0.01 M NaOH + 0.15 M NaCl containing glucose.

To sum up, keeping in mind that the LDR of modern glucose sensors is 1–30 mM, the sensor systems based on MIL-88B(Fe) require further optimization. For instance, the use of a flow-limiting membrane could be considered in the future to expand the linear detection range of the sensors based on MIL-88B(Fe) composites. However, it should be noted that the high anodic polarization used for glucose detection leads to a significant increase in cross-sensitivity; therefore, modifying the MOF composition is necessary to optimize the electroanalytical performance.

Conclusions

For the first time, a series of electrically conductive MIL-88B(Fe)/graphite composites with graphite contents ranging from 12.5 to 75 wt.% was successfully prepared using trinuclear iron(III) acetate as the precursor. According to BET analysis, the specific surface area non‑monotonically decreases from 220 m^2/g for MIL-88B(Fe) to 15.2 m^2/g for MIL‑88B(Fe)/graphite (75 wt.%), while the calculated QSDFT pore diameter shifts from 4.6 nm for pure MIL-88B(Fe) to a stable 3.1 nm for the composites. Importantly, this suggests that graphite is localized on the external surface of the MOF crystals without significant penetration into the pores. Furthermore, XRD confirmed the absence of secondary iron oxide phases in the proposed synthesis route, indicating the high phase purity of the MIL-88B(Fe)/graphite composites. FTIR spectroscopy of the MIL-88B(Fe)/graphite composites revealed splitting of the carboxylate stretching vibration bands and the appearance of a band at 1688 cm^{-1}, indicating the presence of dangling linkers coordinated to the metal cluster via only one carboxylate group. This is attributed to incomplete substitution of carboxylate fragments during the *in situ* synthesis in the presence of graphite. Raman spectroscopy confirmed the presence of the graphite phase in the composites and showed an increase in graphite defectiveness upon synthesis. The characteristic bands of the terephthalate linker of MIL-88B(Fe) (~1603, 1502, 1427, 1284, and 1132 cm^{-1}) were identified, confirming the preservation of the MOF structure. Scanning electron microscopy showed that aggregates are already formed in the composites at 12.5 wt% graphite, and the particle size exhibits a non‑monotonic behavior reflecting the competition between MOF aggregation and graphite phase distribution. An inverse linear correlation was found between the graphite content and the mass loss in the first de-

composition stage, attributed to dehydration. With increasing graphite weight fraction, the rate of mass loss associated with decarboxylation decreases, and the decomposition intensity regularly diminishes. As the MOF content in the composite increases, both the total number of particles and their degree of aggregation increase. Electrocatalytic activity of MIL-88B(Fe) toward glucose in alkaline medium was observed for the first time; however, further studies are required to improve the sensing performance.

Supporting Information

The Supporting Information is available free at https://ejc.buketov.edu.kz/ejc/article/view/776/419

Funding

This research was supported by a grant from the Russian Science Foundation (RSF), Project No. 26-13-00404 (https://rscf.ru/project/26-13-00404/).

*Author Information**

**The authors' names are presented in the following order: First Name, Middle Name and Last Name*

Rose Baimuratova Kurmangalievna (*corresponding author*) — Candidate of Chemical Sciences, Researcher, Federal Research Center of Problems of Chemical Physics and Medicinal Chemistry Russian Academy of Sciences, Ac. Semenov avenue 1, 142432, Chernogolovka, Moscow region, Russia; e-mail: roz_baz@mail.ru; https://orcid.org/0000-0002-8389-6871

Ravil Nailevich Bazargulov — Student, Department of Fundamental Physical and Chemical Engineering, Lomonosov Moscow State University, 1 Leninskie Gory, Build. 51, 119991 Moscow, Russian Federation; Research Trainee at the Federal Research Center of Problems of Chemical Physics and Medicinal Chemistry, Russian Academy of Sciences, 142432, Chernogolovka, Moscow Region, Russia; e-mail: elektrosolbox@gmail.com

Sofia Alekseevna Kleinikova — Candidate of Chemical Sciences, Junior Researcher, Federal Research Center of Problems of Chemical Physics and Medicinal Chemistry Russian Academy of Sciences, Ac. Semenov avenue 1, 142432, Chernogolovka, Moscow region, Russia; e-mail: s.a.kleinikova@icp.ac.ru; https://orcid.org/0000-0001-7802-4967

Ekaterina Viktorovna Zolotukhina — Doctor of Chemical Sciences, Deputy Director for Research, Head of Laboratory, Federal Research Center of Problems of Chemical Physics and Medicinal Chemistry Russian Academy of Sciences, Ac. Semenov avenue 1, 142432, Chernogolovka, Moscow region, Russia; e-mail: zolek@icp.ac.ru; https://orcid.org/0000-0002-1735-0264

Konstantin Vladimirovich Gor'kov — Candidate of Chemical Sciences, Researcher, Federal Research Center of Problems of Chemical Physics and Medicinal Chemistry Russian Academy of Sciences, Ac. Semenov avenue 1, 142432, Chernogolovka, Moscow region, Russia; e-mail: gorkovk@yandex.ru; https://orcid.org/0000-0003-1946-8597

Mikhail Vladimirovich Zhidkov — Candidate of Technical Sciences, Researcher, Federal Research Center of Problems of Chemical Physics and Medicinal Chemistry Russian Academy of Sciences, Ac. Semenov avenue 1, 142432, Chernogolovka, Moscow region, Russia; e-mail: zhidkov@icp.ac.ru; https://orcid.org/0000-0001-7513-2057

Gulzhian Iskakovna Dzhardimalieva — Doctor of Chemical Sciences, Head of Laboratory of Metallopolymers, Federal Research Center of Problems of Chemical Physics and Medicinal Chemistry Russian Academy of Sciences, Ac. Semenov avenue 1, 142432, Chernogolovka, Moscow region, Russia; Professor, Moscow Aviation Institute (National Research University), 4 Volokolamskoe Highway, 125993, Moscow, Russia; e-mail: dzhardim@icp.ac.ru; https://orcid.org/0000-0002-4727-8910

Author Contributions

The manuscript was written through contributions of all authors. All authors have given approval to the final version of the manuscript. CRediT: **Baimuratova Rose Kurmangalievna** conceptualization, methodology, data curation, investigation, writing-original draft; **Ravil Nailevich Bazargulov** investigation, valida-

tion, visualization; **Sofia Alekseevna Kleinikova** investigation, visualization, writing-original draft; **Ekaterina Viktorovna Zolotukhina** methodology, data curation, supervision, writing-review & editing; **Konstantin Vladimirovich Gor'kov** investigation, data curation, validation; **Mikhail Vladimirovich Zhidkov** investigation, data curation; **Gulzhian Iskakovna Dzhardimalieva** conceptualization, data curation, funding acquisition, resources, supervision, writing-review & editing.

Acknowledgments

Low-temperature nitrogen adsorption and IR spectroscopy were carried out by using the equipment of the Multi-User Analytical Center of Federal Research Center of Problems of Chemical Physics and Medicinal Chemistry Russian Academy of Sciences.

Conflicts of Interest

The authors declare no conflict of interest.

References

1 Raveendran, A. V., Chandran, M., & Dhanusuraman, R. (2023). A comprehensive review on the electrochemical parameters and recent material development of electrochemical water splitting electrocatalysts. *RSC Advances*, *13*, 3843–3876. https://doi.org/10.1039/d2ra07642j

2 Water electrolysis: From textbook knowledge to the latest scientific strategies and industrial developments. (2022). *Chemical Society Reviews*, *51*, 4583–4762. https://doi.org/10.1039/d0cs01079k

3 Zhai, Q., Huang, H., Lawson, T., Xia, Z., Giusto, P., Antonietti, M., Jaroniec, M., Chhowalla, M., Baek, J. -B., Liu, Y., Qiao, S., & Dai, L. (2024). Recent Advances on Carbon-Based Metal-Free Electrocatalysts for Energy and Chemical Conversions. *Advanced Materials*, *36*. https://doi.org/10.1002/adma.202405664

4 Fan, L., Xia, C., Yang, F., Wang, J., Wang, H., & Lu, Y. (2020). Strategies in catalysts and electrolyzer design for electrochemical CO2 reduction toward C2+ products. *Science Advances*, *6*. https://doi.org/10.1126/sciadv.aay3111

5 Overa, S., Ko, B., Zhao, Y., & Jiao, F. (2022). Electrochemical Approaches for CO2 Conversion to Chemicals: A Journey toward Practical Applications. *Accounts of chemical research*. https://doi.org/10.1021/acs.accounts.1c00674

6 Singh, S., Yadav, R. K., Kim, T. W., Singh, C., Singh, P., Chaubey, S., Rose, B., Gulzhian, D., & Khare, P. (2022). In Situ Prepared NRCPFs as Highly Active Photo Platforms for in Situ Bond Formation Between Aryldiazonium Salts and Heteroarenes. *Photochemistry and Photobiology*, *98*(4), 748–753. https://doi.org/10.1111/php.13639

7 Ferreira, A. P. R. A., Oliveira, R. C. P., Mateus, M., & Santos, D. (2023). A Review of the Use of Electrolytic Cells for Energy and Environmental Applications. *Energies*. https://doi.org/10.3390/en16041593

8 Azari, P., Hasheminejad, H., & Zarean Mousaabadi, K. (2025). Synthesis and characterization of MIL-88 A (Fe)/C composite for treatment of dairy factory's wastewater by enhanced electro-Fenton method. *Scientific Reports*, *15*(1), 8503. https://doi.org/10.1038/s41598-025-92765-4

9 Dhara, K., & Mahapatra, D. (2017). Electrochemical nonenzymatic sensing of glucose using advanced nanomaterials. *Microchimica Acta*, *185*, 1–32. https://doi.org/10.1007/s00604-017-2609-1

10 Li, H., Xiao, N., Jiang, M., Long, J., Li, Z., & Zhu, Z. (2024). Advances of Transition Metal-Based Electrochemical Nonenzymatic Glucose Sensors for Glucose Analysis: A Review. *Critical Reviews in Analytical Chemistry*, *55*, 1099–1135. https://doi.org/10.1080/10408347.2024.2339955

11 Zhang, J., Xiong, Q., & Xu, J. (2024). Research progress in non-precious metal oxide/compound-based electrodes for non-enzymatic electrochemical glucose sensor applications. *Materials Science in Semiconductor Processing*. https://doi.org/10.1016/j.mssp.2024.108643

12 Batten, S. R., Champness, N. R., Chen, X. -M., Garcia-Martinez, J., Kitagawa, S., Öhrström, L., O'Keeffe, M., Paik Suh, M., & Reedijk, J. (2013). Terminology of metal–organic frameworks and coordination polymers (IUPAC Recommendations 2013). *Pure and Applied Chemistry*, *85*(8), 1715–1724. https://doi.org/10.1351/PAC-REC-12-11-20

13 Gao, Q., Sheng, Q., Zhang, S., & Tang, Y. (2025). Recent trends on MIL-88(Fe) metal–organic frameworks: Synthesis and applications in pollutant removal and detection. *RSC Advances*, *15*(32), 26184–26200. https://doi.org/10.1039/D5RA03049H

14 Channab, B. -E., El Ouardi, M., Ait Layachi, O., Marrane, S. E., El Idrissi, A., BaQais, A., & Ait Ahsaine, H. (2023). Recent trends on MIL-Fe metal–organic frameworks: Synthesis approaches, structural insights, and applications in organic pollutant adsorption and photocatalytic degradation. *Environmental Science: Nano*, *10*(11), 2957–2988. https://doi.org/10.1039/d3en00332a

15 Huang, Q., Zeb, A., Xu, Z., Sahar, S., Zhou, J. -E., Lin, X., Wu, Z., Reddy, R. C. K., Xiao, X., & Hu, L. (2023). Fe-based metal-organic frameworks and their derivatives for electrochemical energy conversion and storage. *Coordination Chemistry Reviews*, *494*, 215335. https://doi.org/10.1016/j.ccr.2023.215335

16 Morozan, A., & Jaouen, F. (2012). Metal organic frameworks for electrochemical applications. *Energy & Environmental Science*, *5*(11), 9269–9290. https://doi.org/10.1039/C2EE22989G

17 Ishimoto, T., Ogura, T., Koyama, M., Yang, L., Kinoshita, S., Yamada, T., Tokunaga, M., & Kitagawa, H. (2013). A Key Mechanism of Ethanol Electrooxidation Reaction in a Noble-Metal-Free Metal–Organic Framework. *The Journal of Physical Chemistry C*, *117*(20), 10607–10614. https://doi.org/10.1021/jp4031046

18 Serre, C., Mellot-Draznieks, C., Surblé, S., Audebrand, N., Filinchuk, Y., & Férey, G. (2007). Role of solvent-host interactions that lead to very large swelling of hybrid frameworks. *Science*, *315*(5820), 1828–1831.

19 Horcajada, P., Serre, C., Maurin, G., Ramsahye, N. A., Balas, F., Vallet-Regí, M., Sebban, M., Taulelle, F., & Férey, G. (2008). Flexible Porous Metal-Organic Frameworks for a Controlled Drug Delivery. *Journal of the American Chemical Society*, *130*(21), 6774–6780. https://doi.org/10.1021/ja710973k

20 Ma, M., Bétard, A., Weber, I., Al-Hokbany, N. S., Fischer, R. A., & Metzler-Nolte, N. (2013). Iron-Based Metal–Organic Frameworks MIL-88B and NH2-MIL-88B: High Quality Microwave Synthesis and Solvent-Induced Lattice "Breathing". *Crystal Growth & Design*, *13*(6), 2286–2291. https://doi.org/10.1021/cg301738p

21 Gao, F., Yan, R., Shu, Y., Cao, Q., & Zhang, L. (2022). Strategies for the application of metal–organic frameworks in catalytic reactions. *RSC Advances*, *12*(16), 10114–10125. https://doi.org/10.1039/D2RA01175A

22 Zhu, Q. -L., & Xu, Q. (2014). Metal–organic framework composites. *Chem. Soc. Rev.*, *43*(16), 5468–5512. https://doi.org/10.1039/C3CS60472A

23 Liew, A. S. Y., Nguang, S. Y., Minggu, L. J., Tahir, N., & Moh, P. Y. (2021). Graphene oxide incorporated amino-functionalized iron terephthalate composite as a heterogeneous Fenton-like catalyst. *Journal of the Chinese Chemical Society*, *68*(10), 1887–1896. https://doi.org/10.1002/jccs.202100183

24 Elmowafy, M. E., Zorainy, M., Abuzalat, O., Baraka, A., Sadek, R., & Tantawy, H. (2025). A novel double-layer MIL-88B (Fe/Co)/RGO composite as a superior microwave shielding material. *Journal of Nanoparticle Research*, *27*(8), 211. https://doi.org/10.1007/s11051-025-06393-0

25 Abazari, R., Sanati, S., & Morsali, A. (2022). Mixed metal Fe2Ni MIL-88B metal–organic frameworks decorated on reduced graphene oxide as a robust and highly efficient electrocatalyst for alkaline water oxidation. *Inorganic Chemistry*, *61*(8), 3396–3405.

26 Jia, D., Shen, Z., Lv, Y., Chen, Z., Li, H., Yu, Y., Qiu, J., & He, X. (2024). In situ electrochemical tuning of MIL-88B (V)@ rGO into amorphous V2O5@ rGO as cathode for high-performance aqueous zinc-ion battery. *Advanced Functional Materials*, *34*(2), 2308319. https://doi.org/10.1002/adfm.202308319

27 Zhang, C., Weiqiang, H., Jiang, H., Chang, J. -K., Zheng, M. -S., Wu, Q., & Dong, Q. (2017). Electrochemical performance of MIL-53(Fe)@RGO as an Organic Anode Material for Li-ion Batteries. *Electrochimica Acta*, *246*. https://doi.org/10.1016/j.electacta.2017.06.059

28 Jin, Y., Zhao, C., Lin, Y., Wang, D., Chen, L., & Shen, C. (2017). Fe-Based Metal-Organic Framework and Its Derivatives for Reversible Lithium Storage. *Journal of Materials Science & Technology*, *33*(8), 768–774. https://doi.org/10.1016/j.jmst.2016.11.021

29 Zhang, H., Chen, S., Zhang, H., Fan, X., Gao, C., Yu, H., & Quan, X. (2019). Carbon nanotubes-incorporated MIL-88B-Fe as highly efficient Fenton-like catalyst for degradation of organic pollutants. *Frontiers of Environmental Science & Engineering*, *13*(2), 18. https://doi.org/10.1007/s11783-019-1101-z

30 Qin, W., He, L., Zhang, Y., Li, B., Han, L., & Xu, Y. (2024). Synchronous wrapping and inward-etching strategy on constructing yolk-shell MIL-88A@ NiFe-PB heterostructures for electrochemical non-enzymatic glucose detection. *Microchemical Journal*, *196*, 109641. https://doi.org/10.1016/j.microc.2023.109641

31 Baimuratova, R. K., Zhinzhilo, V. A., Uflyand, I. E., Dmitriev, A. I., Zhidkov, M. V., Ovanesyan, N. S., Kugabaeva, G. D., & Dzhardimalieva, G. I. (2023). Low-Temperature Synthesis of Metal–Organic Coordination Polymers Based on Oxo-centered Iron Complexes: Magnetic and Adsorption Properties. *Russian Journal of Physical Chemistry A*, *97*(4), 735–748. https://doi.org/10.1134/S0036024423040064

32 Sidorov, V. I., Baimuratova, R. K., Korchagin, D. V., Ivanov, A. I., Kydralieva, K. A., & Dzhardimalieva, G. I. (2024). Magnetically Separable Fe3O4/γ-Fe2O3@MIL-88b(Fe) and Fe3O4/γ-Fe2O3@NH2-MIL-88b(Fe) Composites for the Photocatalytic Degradation of Congo Red Dye. *Eurasian Journal of Chemistry*, *29*(3 (115)), 130–147. https://doi.org/10.31489/2959-0663/3-24-5

33 Collins, T. J. (2007). ImageJ for microscopy. *Biotechniques*, *43*(sup1), S25–S30.

34 Chen, Z., Hanna, S. L., Redfern, L. R., Alezi, D., Islamoglu, T., & Farha, O. K. (2019). Reticular chemistry in the rational synthesis of functional zirconium cluster-based MOFs. *Coordination Chemistry Reviews*, *386*, 32–49. https://doi.org/10.1016/j.ccr.2019.01.017

35 Kumar, P., & Bohidar, H. B. (2010). Aqueous dispersion stability of multi-carbon nanoparticles in anionic, cationic, neutral, bile salt and pulmonary surfactant solutions. *Colloids and Surfaces A: Physicochemical and Engineering Aspects*, *361*(1–3), 13–24.

36 Agola, P., & Taddei, M. (2026). A water-based synthetic route to the metal–organic framework UiO-66 starting from PET-derived terephthalate esters. *RSC Sustainability*, *4*(1), 466–476. https://doi.org/10.1039/D5SU00463B

37 Sánchez-Sánchez, M., Getachew, N., Díaz, K., Díaz-García, M., Chebude, Y., & Díaz, I. (2015). Synthesis of metal–organic frameworks in water at room temperature: Salts as linker sources. *Green Chemistry*, *17*, 1500–1509. https://doi.org/10.1039/c4gc01861c

38 Kondo, Y., Kuwahara, Y., Mori, K., & Yamashita, H. (2021). Dual role of missing-linker defects terminated by acetate ligands in a zirconium-based MOF in promoting photocatalytic hydrogen peroxide production. *The Journal of Physical Chemistry C*, *125*(51), 27909–27918. https://doi.org/10.1021/acs.jpcc.1c07735

39 Shearer, G. C., Chavan, S., Bordiga, S., Svelle, S., Olsbye, U., & Lillerud, K. P. (2016). Defect Engineering: Tuning the Porosity and Composition of the Metal–Organic Framework UiO-66 via Modulated Synthesis. *Chemistry of Materials*, *28*(11), 3749–3761. https://doi.org/10.1021/acs.chemmater.6b00602

40 Pangestu, A., Lestari, W. W., Wibowo, F. R., & Larasati, L. (2022). Green Electro-Synthesized MIL-101(Fe) and Its Aspirin Detoxification Performance Compared to MOF-808. *Journal of Inorganic and Organometallic Polymers and Materials*, *32*(5), 1828–1839. https://doi.org/10.1007/s10904-022-02235-x

41 Chávez, A. M., Rey, A., López, J., Álvarez, P., & Beltrán, F. (2021). Critical aspects of the stability and catalytic activity of MIL-100(Fe) in different advanced oxidation processes. *Separation and Purification Technology*, *255*. https://doi.org/10.1016/j.seppur.2020.117660

42 Wang, K. -Y., Yang, Z., Zhang, J., Banerjee, S., Joseph, E., Hsu, Y. -C., Yuan, S., Feng, L., & Zhou, H. (2022). Creating hierarchical pores in metal–organic frameworks via postsynthetic reactions. *Nature Protocols*, *18*, 604–625. https://doi.org/10.1038/s41596-022-00759-7

43 Schneemann, A., Bon, V., Schwedler, I., Senkovska, I., Kaskel, S., & Fischer, R. A. (2014). Flexible metal–organic frameworks. *Chem. Soc. Rev.*, *43*(16), 6062–6096. https://doi.org/10.1039/C4CS00101J

44 Li, Y., Wang, Y., Fan, W., & Sun, D. (2022). Flexible metal–organic frameworks for gas storage and separation. *Dalton Transactions*, *51*(12), 4608–4618. https://doi.org/10.1039/D1DT03842G

45 Pallach, R., Keupp, J., Terlinden, K., Frentzel-Beyme, L., Kloß, M., Machalica, A., Kotschy, J., Vasa, S. K., Chater, P. A., Sternemann, C., Wharmby, M. T., Linser, R., Schmid, R., & Henke, S. (2021). Frustrated flexibility in metal-organic frameworks. *Nature Communications*, *12*(1), 4097. https://doi.org/10.1038/s41467-021-24188-4

46 Mellot-Draznieks, C., Serre, C., Surblé, S., Audebrand, N., & Férey, G. (2005). Very Large Swelling in Hybrid Frameworks: A Combined Computational and Powder Diffraction Study. *Journal of the American Chemical Society*, *127*(46), 16273–16278. https://doi.org/10.1021/ja054900x

47 Ye, Z., Zhang, W., Lanzalaco, S., Zhao, L., Sirés, I., Xia, P., Zhai, J., & He, Q. (2023). Ultra-uniform MIL-88B(Fe)/Fe3S4 hybrids engineered by partial sulfidation to boost catalysis in electro-Fenton treatment of micropollutants: Experimental and mechanistic insights. *Chemical Engineering Journal*, *455*, 140757. https://doi.org/10.1016/j.cej.2022.140757

48 Zhang, S., Zhuo, Y., Ezugwu, C. I., Wang, C., Li, C., & Liu, S. (2021). Synergetic Molecular Oxygen Activation and Catalytic Oxidation of Formaldehyde over Defective MIL-88B(Fe) Nanorods at Room Temperature. *Environmental Science & Technology*, *55*(12), 8341–8350. https://doi.org/10.1021/acs.est.1c01277

49 Karagiaridi, O., Vermeulen, N. A., Klet, R. C., Wang, T. C., Moghadam, P. Z., Al-Juaid, S. S., Stoddart, J. F., Hupp, J. T., & Farha, O. K. (2015). Functionalized defects through solvent-assisted linker exchange: Synthesis, characterization, and partial postsynthesis elaboration of a metal–organic framework containing free carboxylic acid moieties. *Inorganic chemistry*, *54*(4), 1785–1790. https://doi.org/10.1021/ic502697y

50 Nakamoto, K. (2009). *Infrared and Raman spectra of inorganic and coordination compounds* (6th ed). Wiley. https://doi.org/10.1002/9780470405840

51 Aizyatullov, A. S., Baimuratova, R. K., Sidorov, V. L., Spirin, M. G., Shilov, G. V., Dremova, N. N., & Dzhardimalieva, G. I. (2026). Engineering TiO2/MIL-88b(Fe) heterostructures for enhanced photocatalytic degradation of organic dyes. *Materials Science in Semiconductor Processing*, *211*, 110725. https://doi.org/10.1016/j.mssp.2026.110725

52 Hollauer, E., Mondragon, M. A., & Castaño, V. M. (2001). Fourier transform infrared and Raman spectra, vibrational assignment and ab initio calculations of terephthalic acid and related compounds. *Spectrochimica Acta Part A: Molecular and Biomolecular Spectroscopy*, *57*(5), 993–1007. https://doi.org/10.1016/s1386-1425(00)00428-5

53 Deacon, G. B., & Phillips, R. J. (1980). Relationships between the carbon-oxygen stretching frequencies of carboxylato complexes and the type of carboxylate coordination. *Coordination chemistry reviews*, *33*(3), 227–250. https://doi.org/10.1016/s0010-8545(00)80455-5

54 Tuinstra, F., & Koenig, J. L. (1970). Raman spectrum of graphite. *The Journal of chemical physics*, *53*(3), 1126–1130. https://doi.org/10.1063/1.1674108

55 Ferrari, A. C., & Robertson, J. (2000). Interpretation of Raman spectra of disordered and amorphous carbon. *Physical review B*, *61*(20), 14095. https://doi.org/10.1103/physrevb.61.14095

56 Nguyen, V. H., Nguyen, T. D., Bach, L. G., Hoang, T., Bui, Q. T. P., Tran, L. D., Nguyen, C. V., Vo, D. -V. N., & Do, S. T. (2018). Effective Photocatalytic Activity of Mixed Ni/Fe-Base Metal-Organic Framework under a Compact Fluorescent Daylight Lamp. *Catalysts*, *8*(11), 487. https://doi.org/10.3390/catal8110487

57 Hadjiivanov, K. I., Panayotov, D. A., Mihaylov, M. Y., Ivanova, E. Z., Chakarova, K. K., Andonova, S. M., & Drenchev, N. L. (2020). Power of infrared and Raman spectroscopies to characterize metal-organic frameworks and investigate their interaction with guest molecules. *Chemical Reviews*, *121*(3), 1286–1424. https://doi.org/10.1021/acs.chemrev.0c00487

58 Banerjee, P. C., Lobo, D. E., Middag, R., Ng, W. K., & Et., A. (2015). Electrochemical Capacitance of Ni-Doped Metal Organic Framework and Reduced Graphene Oxide Composites: More than the Sum of Its Parts. *ACS Applied Materials & Interfaces*. https://doi.org/10.1021/am508119c

59 Guo, M., & Li, H. (2021). The Hydrolyzed Mil-88B(Fe) With Improved Surface Area for High-Capacity Lithium Ion Battery. *Frontiers in Energy Research*, *9*, 781008. https://doi.org/10.3389/fenrg.2021.781008

60 Hou, S., Wu, Y., Feng, L., Chen, W., Wang, Y., Morlay, C., & Li, F. (2018). Green synthesis and evaluation of an iron-based metal–organic framework MIL-88B for efficient decontamination of arsenate from water. *Dalton Transactions*, *47*(7), 2222–2231. https://doi.org/10.1039/C7DT03775A

61 Morsy, M., Hassan, S. S., Shaker, H. M., & Ismail, K. M. (2025). Synthesis and characterization of MIL-88B(Fe) MOF for high-performance humidity sensing. *Sensors and Actuators B: Chemical*, *438*, 137806. https://doi.org/10.1016/j.snb.2025.137806

62 Zorainy, M. Y., Kaliaguine, S., Gobara, M., Elbasuney, S., & Boffito, D. C. (2022). Microwave-Assisted Synthesis of the Flexible Iron-based MIL-88B Metal–Organic Framework for Advanced Energetic Systems. *Journal of Inorganic and Organometallic Polymers and Materials*, *32*(7), 2538–2556. https://doi.org/10.1007/s10904-022-02353-6

63 Xu, B., Yang, H., Cai, Y., Yang, H., & Li, C. (2016). Preparation and photocatalytic property of spindle-like MIL-88B (Fe) nanoparticles. *Inorganic Chemistry Communications*, *67*, 29–31. https://doi.org/10.1016/j.inoche.2016.03.003

64 Bhardwaj, U., Janjani, P., Sharma, R., & Kushwaha, H. S. (2023). Investigation of Single-Metal Fe-Based Metal–Organic Framework as an Electrocatalyst for a Rechargeable Zinc-Air Battery. *Journal of Electronic Materials*, *52*(2), 917–924. https://doi.org/10.1007/s11664-022-10106-x